Flux and Loss Map Based Evaluation of the Efficiency Map of Synchronous Machines

Flux and Loss Map Based Evaluation of the Efficiency Map of Synchronous Machines

Simone Ferrari, *Member, IEEE* Paolo Ragazzo, *Student Member, IEEE* Gaetano Dilevrano, *Student Member, IEEE* Gianmario Pellegrino, *Fellow, IEEE*

***Abstract*—This paper presents a methodology for the efficiency maps evaluation of synchronous electric machines. The procedure is based on the manipulation of flux linkage, iron and PM loss maps obtained via 2D magneto-static Finite-Element Analysis. The paper thoroughly describes the procedure and its key computational steps, all referring to open-source Matlab code available to the public. A method for iron loss evaluation from magneto-static FEA is proposed, valid for both sinusoidal and PWM supply. Experimental results are provided for the validation of single loss terms calculation and for the whole efficiency map, with reference to an interior permanent magnet machine designed for traction. FEA evaluation of PWM supply conditions relies on the off-line computation of the motor phase currents using a custom PLECS model of the drive, still flux-map based. This step of the procedure is also validated experimentally. The proposed methodology covers permanent magnet synchronous and synchronous reluctance machines, and finds prominent application in the automotive field, for traction and on-board generation.**

I. Introduction

Inverter controlled synchronous machines are the state-of-the-art solution for high-efficiency industrial applications and electrified vehicular traction [1] [2]. Synchronous machines can be divided into several categories, mainly depending on the type of rotor. Based on the ratio of permanent magnet (PM) to reluctance torque, the vast category of Permanent Magnet Synchronous Machines (PMSMs) ranges from Surface-mounted PM (SPM) machines [3] to Interior Permanent Magnet (IPM) machines [4], to PM-assisted Synchronous Reluctance (PM-SyR) machines. Synchronous Reluctance (SyR) machines are appreciated in industry applications and in traction [5], for their manufacturing simplicity and high efficiency, if compared to asynchronous motors [6]. The efficiency map is one key performance metric for those applications where a variety of working points is explored on the torque-speed plane, such as traction [7].

The paper proposes a comprehensive method to compute the efficiency map of a PMSM based on FEA-evaluated flux and loss maps, and it is organized as follows. Section II introduces the flux-map based steady-state model of the machine. Section III discusses how the different loss terms are evaluated using magneto-static FEA. Section IV describes the evaluation of the efficiency maps. Section V reports on the experimental results and section VI addresses the evaluation and validation of PWM generated loss terms. The case of study is the PM-SyR machine described in Fig. 1 and Table I. Following the conference work [8], the new contributions of this paper are:

- the experimental validation of the FEA calculated efficiency maps.
- a new methodology to account for PWM losses in the windings and in iron and its validation.
- the flux map based PLECS [9] circuital model of the e-drive for the evaluation of the PWM phase current waveforms fed to the FEA model for PWM loss evaluation.
- the experimental validation of the current waveforms from the PLECS model.

All the described procedures are included in SyR-e [10], the open-source environment for electrical machines design and FEA evaluation developed in Matlab and FEMM [11]. The proposed method is a fast and largely available computation tool that can find useful application both at machine design level and at power-train and vehicle system level studies. The flux-map approach makes the proposed procedure valid in general for three-phase synchronous machines.

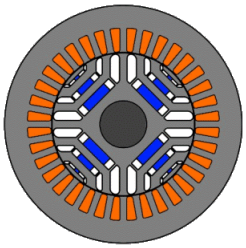

Fig. 1. Reference PM-SyR machine.

TABLE I
Reference machine ratings

Nominal current	i_{nom}	22	[Apk]
Max current	i_{max}	44	[Apk]
Nominal torque	T_{nom}	19	[Nm]
Max torque	T_{max}	43	[Nm]
DC link voltage	V_{DC}	310	[V]
Nominal speed	n_{nom}	2500	[rpm]
Max speed	n_{max}	9000	[rpm]
Nominal power	P_{nom}	5	[kW]
Max power	P_{max}	11.5	[kW]

II. Flux map based machine model

A. Steady-State Model of the AC Machine

The steady-state model of the AC synchronous machine is represented by (1)-(2) and by the circuit of Fig. 2.

$$v_{dq} = R_s \cdot i_{dq} + j \cdot \omega \cdot \lambda_{dq} \tag{1}$$

The complex notation is adopted, where $v_{dq} = v_d + j \cdot v_q$ is the dq voltage space vector, $i_{dq} = i_d + j \cdot i_q$ is the dq current, R_s is the phase resistance, ω is the angular frequency and $\lambda_{dq} = \lambda_d + j \cdot \lambda_q$ is the dq flux linkage. To account for the aggregate of iron and PM losses, the R_{Fe} branch is added, draining the equivalent loss current $i_{dq}^{Fe} = i_d^{Fe} + j \cdot i_q^{Fe}$. The stator current vector is:

$$i_{dq} = i_{dq}^{m} + i_{dq}^{Fe} \tag{2}$$

S. Ferrari, P. Ragazzo, G. Dilevrano and G. Pellegrino are with the Department of Energy *Galileo Ferraris*, Politecnico di Torino, Turin, Italy (e-mails: simone.ferrari@polito.it, paolo.ragazzo@polito.it, gaetano.dilevrano@polito.it and gianmario.pellegrino@polito.it)

where the magnetizing current $i_{dq}^m = i_d^m + j \cdot i_q^m$ is defined. The flux linkage vector components are a function of the magnetizing current vector according to the flux map operators $\mathbf{\Lambda}_d$ and $\mathbf{\Lambda}_q$ represented in Fig. 3. Note that R_{Fe} is not a constant value but depends on the operating point according to the loss map described later in the paper. The power at the motor terminals is defined as:

$$P_{elt} = \mathbb{R}\left(\frac{3}{2} \cdot v_{dq} \cdot i_{dq}^*\right) = P_{Cu} + P_{Fe} + P_{PM} + T_{em} \cdot \frac{\omega}{p} \quad (3)$$

where $\mathbb{R}$ indicates the real part of the complex number and the superscript "$*$"is the complex conjugate operator. The input electrical power equals the sum of copper P_{Cu}, iron P_{Fe}, PM P_{PM} loss and the product between electromagnetic torque T_{em} and mechanical speed $\frac{\omega}{p}$. Substituting (1) and (2) in (3), the right side terms of the equation become:

$$P_{Cu} = \frac{3}{2} \cdot R_s \cdot \left(i_d^2 + i_q^2\right) = \frac{3}{2} \cdot R_s \cdot |i_{dq}|^2 \quad (4)$$

$$P_{Fe} + P_{PM} = \frac{3}{2}\omega\left(\lambda_d i_q^{Fe} + \lambda_q i_d^{Fe}\right) = \mathbb{R}\left[\frac{3}{2} \cdot (j\omega\lambda_{dq}) \cdot \left(i_{dq}^{Fe}\right)^*\right] \quad (5)$$

$$T_{em} = \frac{3}{2} p \cdot \left(\lambda_d i_q^m - \lambda_q i_d^m\right) \quad (6)$$

The shaft torque T is obtained by subtracting the mechanical loss P_{mech} contribution from the electromagnetic torque:

$$T = T_{em} - \frac{P_{mech}}{\frac{\omega}{p}} \quad (7)$$

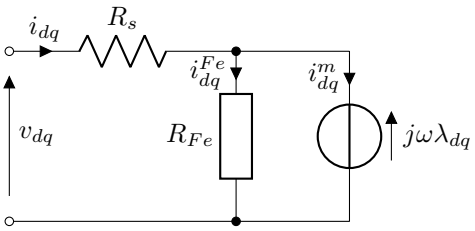

Fig. 2. Steady state equivalent circuit model of the machine

B. Flux maps computation

Flux maps are obtained by multi-step FEA simulations on a regular grid in the (i_d^m, i_q^m) plane. The number of points of the grid represents a trade-off between accuracy and computational time. Here 15x15 points were used. The precautions adopted for a fast evaluation of the maps are:

- Use of 2D FEA and off-line evaluation of end-turn effects.
- Magneto-static FEA with sequenced rotor positions instead of transient FEA.
- Geometric symmetry: one pole is simulated for machines with anti-periodic symmetry. More than one pole might be necessary for machines with different properties.
- Electric symmetry: simulation of a submultiple of the electrical period, which is typically $\frac{1}{6}$ of the electrical period for 3-phase distributed windings [12].

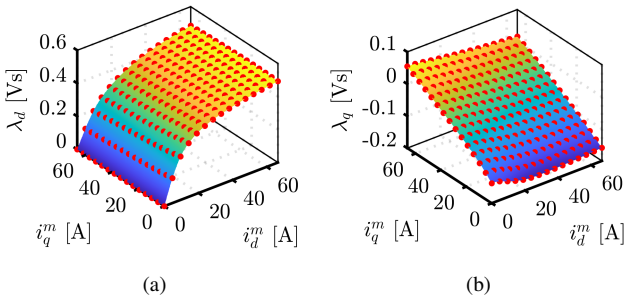

(a) (b)

Fig. 3. Flux maps: d-axis flux linkage (a) and q-axis flux linkage (b). Red points represents the FEA simulations, while the surfaces are re-interpolated over a finer 256x256 grid.

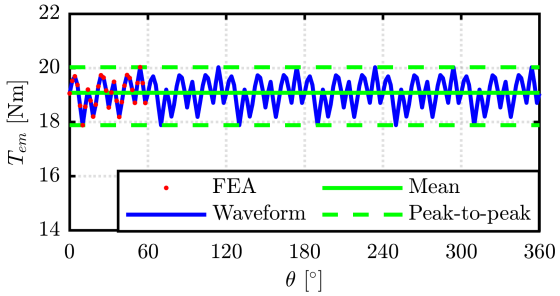

Fig. 4. Torque waveform simulating 30 rotor positions on 60 electrical degrees: FEA results (red dots) and reconstructed waveform (blue line).

Fig. 4 shows the torque waveform computed at $i_d^m = 16\,\text{A}$ and $i_q^m = 15\,\text{A}$ for the benchmark motor, with evidence of simulated rotor positions (red dots) and waveform reconstruction over one pole-pair pitch. The dq flux linkage components from the same simulated points are averaged and saved in the flux maps. Other representative quantities such as torque average and peak-to-peak values or harmonic components are mapped alongside the flux maps.

C. Flux maps organization

The flux maps are 2D matrices function of the i_d^m, i_q^m grid called $\mathbf{I}_d^m$ (repetition of the vector of i_d^m by rows) and $\mathbf{I}_q^m$ (repetition of the vector of i_q^m by columns). The capital bold font notation will be used for indicating a map in the dq current domain. As said, the 2D static FEA simulation is run on a number of rotor positions (say 10 or 30) for each point of the current grid, and the average values of dq flux linkage are saved to populate the matrices $\mathbf{\Lambda}_d(i_d^m, i_q^m)$ and $\mathbf{\Lambda}_q(i_d^m, i_q^m)$.

As the flux maps are function the PM temperature, they must be re-computed for each temperature value of interest.

The same data organization is adopted for the average electromagnetic torque $\mathbf{T}_{em}(i_d^m, i_q^m)$ and the peak-to-peak torque ripple $\mathbf{\Delta T}_{em}(i_d^m, i_q^m)$ maps.

The flux maps evaluation is defined as an "embarrassingly parallel problem", since the computation of one current point is independent from the other points. For this reason, parallel computing is adopted to speed-up the evaluation. For instance, the flux maps reported in Fig. 3 refer to a 15x15 grid with

30 rotor position on 60 electrical degrees, evaluated in less than 30 minutes using a workstation with Intel Xeon E5-2690 v4 CPU, 14 cores and 32GB RAM. A lower number rotor positions is sufficient for flux linkage and torque maps evaluation: with 10 rotor positions the same flux maps are obtained in circa 10 minutes. Peak-to-peak torque ripple mapping, or iron loss suggests the use of a higher angular resolution, as explained in the following.

III. Loss under Sinusoidal and PWM supply

This section addresses how the various loss terms are evaluated, including the effects of harmonic loss. Iron and PM loss is evaluated by direct manipulation of the FEMM field solution for each mesh element, under sinusoidal or PWM current supply.

A. Hysteresis loss estimation

Hysteresis loss is associated to the area traced by the major and minor loops in the B-H plane, as defined in Fig. 5. The major loop is the full-amplitude cycle centered into the origin and travelled at the fundamental frequency of supply of the machine; this is what happens for example in the center of one stator tooth. Minor loops are causes by harmonics of higher order of the flux density waveform, as it happens for example in the stator back-iron example of Fig. 6. The minor loop flux density bias B_{DC} is the center value of the minor loop, defined in Fig. 5. This is particularly evident in the rotor point example in Fig. 6.
In a PMSM, the stator iron sees both major and minor loops already under sinusoidal supply, whereas the rotor sees minor loops with significant DC bias.

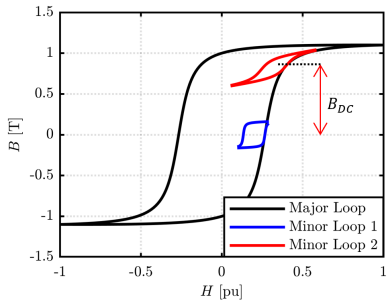

Fig. 5. Hysteresis loops in the BH plane. Fundamental loop in black, minor loops without and with DC-bias are respectively in blue and red.

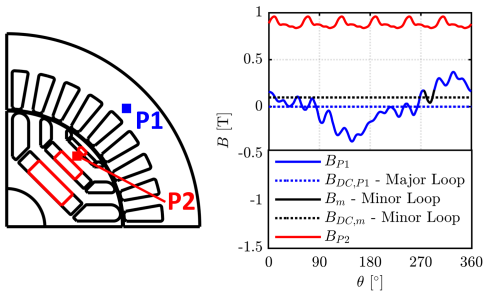

Fig. 6. Flux density waveforms over an electric period of a stator (P1) and a rotor (P2) mesh nodes.

Moreover, currents with PWM ripple produce further rippling of the flux density waveforms, emphasizing the minor loop contribution both in stator and rotor. Notably, the area of a hysteresis loop with fixed flux density amplitude is progressively enlarged by the DC offset up to a certain DC value [13], and this must be accounted for into loss evaluation [14].

The Steinmetz equation of reference is (8), expressing the specific core loss in (W/kg).

$$p_{Fe} = k_h \cdot f^{\alpha} B^{\beta} + k_e \cdot (fB)^2 \tag{8}$$

The coefficients of the equation are obtained by fitting the datasheet loss curves. For the M330-50A steel grade in use, the coefficients of the hysteresis component of (8) are $k_h = 7.55e^{-3}$, $k_e = 6.36e^{-5}$, $\alpha = 1.30$ and $\beta = 1.80$. The second term deals with eddy current loss.

The formulation (8) is enhanced for the hysteresis part in [15] with the improved generalized Steinmetz equation (iGSE). The iGSE method estimates the iron loss for non-sinusoidal current waveforms by contemplating the major and minor hysteresis loops. Equation (9) is applied to each j-th element of the mesh to retrieve the hysteresis loss, where j goes from 1 to the number of mesh elements N.

$$p'_{h,j} = \frac{1}{T} \int_0^T k_i \left| \frac{dB}{dt} \right|^{\alpha} (\Delta B)^{\beta - \alpha} \tag{9}$$

ΔB is the peak-to-peak flux density of the considered loop, $\frac{dB}{dt}$ is the flux density derivative in the simulated time interval T. The subscript j refers to the j-th mesh element. The total hysteresis loss is obtained as sum of the N terms time the mass of each mesh element. The parameter k_i of (9) is obtained from Steinmetz parameters according to (10).

$$k_i = \frac{k_h}{(2\pi)^{\alpha-1} \int_0^{2\pi} |\cos\theta|^{\alpha} 2^{\beta-\alpha} d\theta} \tag{10}$$

The beginning of a minor loop is detected as change in the slope, while its end is fixed where the flux density rises back to the same value where it started decreasing. With the same principle, also nested minor loops are detected.

Among the most appreciated merits, this method can evaluate the loss for any flux waveform with no extra material parameters than the Steinmetz ones, that is using just the loss curves of the material, with no further tests needed, as in other methods in literature [16] [17].

The downside of iGSE is that the core losses variation related to the DC bias is neglected. Here, such a limitation is overcome with a parametric approach based on [18]. The multiplicative factor k_{DC} is applied to the loss of each minor loop integral, function of the respective DC bias. Experimental tests for different iron materials indicated the accuracy of the general law (11) to depict the DC bias effect [18].

$$p_{h,j} = p'_{h,j} \cdot k_{DC} = p'_{h,j} \cdot (0.65 \cdot B_{DC}^{2.1} + 1) \tag{11}$$

where the hysteresis loss of a general element $p_{h,j}$ is calculated from the loss without DC bias $p'_{h,j}$ (9) and from B_{DC}. This approach is adopted for its simplicity and accuracy, among others reviewed [19].

Concerning the simulation setup, one period of fundamental frequency is required to describe the flux density waveforms comprehensively [15]. For the sake of computational time minimization, the symmetry of such waveforms is used. As displayed in Fig. 6, rotor and stator waveforms can be described respectively using 60° and 180° (odd symmetry) electrical degrees. Therefore, the FEA simulations are limited to a rotor excursion of 180° and manipulated for full period reconstruction. When the PWM effect is accounted for, the time step and corresponding rotor angular step must be reduced for increased time resolution.

B. Eddy current loss in the iron

Eddy current loss benefits of superposition properties. Therefore, the flux density waveform of each mesh element is decomposed in harmonic components using the Fast Fourier Transform (FFT) and loss P_e is obtained with the equations (12) (13) .

$$P_e = \sum_{j=1}^{N} m_j \cdot p_{e,j} \qquad p_{e,j} = k_e \sum_{k=1}^{n} f_k^2 B_k^2 \quad (12,\ 13)$$

where $j = 1 \dots N$ indicates the mesh element number, k_e is the eddy-current coefficient of the Steinmetz equation for the M330-50A grade, m_j is the mass corresponding to the element, f_k and B_k are the frequency and the flux density amplitude of the k-th harmonic component.

C. Iron loss map and speed adjustment

The iron losses with sinusoidal (fundamental) excitation are mapped over the (i_d^m, i_q^m) domain, in similar fashion of the flux maps, at a single speed value n_0. The two maps $\mathbf{P}_{h,0}$ and $\mathbf{P}_{e,0}$ represent the hysteresis and eddy-current loss respectively, function of i_{dq}^m, for the frequency $f_0 = n_0 \cdot \frac{60}{p}$. To compute iron loss at a different speed (i.e. different fundamental frequency), the values are rescaled according to the frequency coefficients of the Steinmetz equation:

$$\mathbf{P}_{Fe} = \mathbf{P}_{h,0} \cdot \left(\frac{f}{f_0}\right)^{\alpha} + \mathbf{P}_{e,0} \cdot \left(\frac{f}{f_0}\right)^{2} \quad (14)$$

PWM excited iron loss are evaluated using the same modified iGSE approach through dedicated FEA simulations at the target speed and dq current values, with PWM ripple superimposed to the motor phase currents. This will be addressed in Section VI.

D. Permanent Magnets Loss

Permanent magnet losses are caused by the eddy current circulation in the PM regions and they are calculated by means of FFT, as discussed for the eddy current loss in the iron. To comply with the use of magneto static FEA, the assumption is made to neglect the effect of the eddy currents on the flux distribution. This is valid for IPM and PM-SyR machines and conservative but not always accurate for SPM machines. Another simplifying and conservative assumption is to consider PM loss proportional to f^2, which strongly simplifies data manipulation. Following the assumptions, the PM loss map with sinusoidal excitation $\mathbf{P}_{PM,0}$ at a single speed n_0 are computed over the (i_d^m, i_q^m) grid and then scaled according to speed according to the square of the respective fundamental frequency values:

$$\mathbf{P}_{PM} = \mathbf{P}_{PM,0} \cdot \left(\frac{f}{f_0}\right)^{2} \quad (15)$$

E. AC Copper Loss

The AC winding loss is caused by skin and proximity effects. This is of particular importance for traction motors using hairpin windings with copper bars of large cross section, rather then bundles of wires. The machine under test has stranded conductors, but the method in use is of general validity.

The AC loss factor k_{AC} is defined as the ratio between AC and DC copper loss under sinusoidal supply at frequency f (Hz) (16).

$$k_{AC}(f, \Theta_{Cu}) = \frac{P_{Cu,AC}}{P_{Cu,DC}} \quad (16)$$

For fixed slot and conductor geometries, k_{AC} is a function of the frequency f and the copper temperature. Therefore, the winding resistance R_s is adjusted to account for the AC effect as (17).

$$R_s = R_{s,L} \cdot k_{AC} + R_{s,end} \quad (17)$$

where the k_{AC} is applied to the resistance of the active parts $R_{s,L}$. Notice that the end-winding resistance $R_{s,end}$ value is assumed to be not affected by the AC factor in case of stranded conductors. The k_{AC} factor is computed through linear time-harmonic FEA simulations of the slot. The slot model of the motor under test is reported in Fig. 7. First, the DC copper loss $P_{Cu,DC}$ are computed from FEA model. Then, several combinations of frequency and temperature are simulated to compute AC loss $P_{Cu,AC}$ and finally the AC factor (16). The results from the benchmark motor are reported in Fig. 7a. As expected, the AC factor is small: below 5% for the considered PM-SyR motor if the fundamental frequency is considered (maximum speed of 9000 rpm corresponds to 300 Hz). This is in line with the use of stranded conductors of small cross section (1.2 mm diameter).

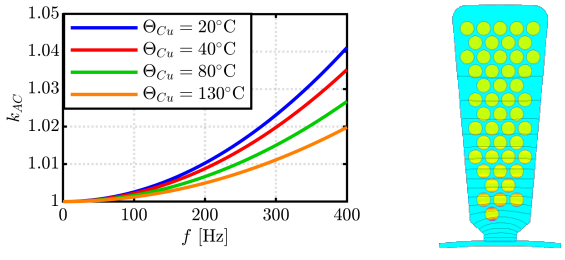

(a) (b)

Fig. 7. AC factor function of the frequency, for different winding temperature (a) and slot model solved at 300 Hz and 20°C.

F. PWM loss in copper

To include the PWM effect, in Section VI-B, the factor k_{AC} is computed for a wider range of frequencies. The frequency range must include all the significant current harmonics, thus the maximum frequency should be greater than twice the switching frequency. Copper loss is calculated accordingly 18.

$$P_{Cu} = \frac{3}{2}\sum_{k=1}^{n}(R_{s,L}\cdot k_{AC,k} + R_{s,end})\cdot {I_k}^2 \qquad (18)$$

where the $k_{AC,k}$ refers to the k-th current harmonic I_k.

G. Mechanical Loss

Mechanical losses are not easy to estimate beforehand, but they can be expressed as a polynomial function of the rotor speed. The literature divides mechanical loss into bearing loss, proportional to speed, and windage loss, proportional to the cubic power of the speed. In the following, mechanical losses are modeled with (19), where the factors $a = 0.26$ nW/rpm^3 (bearing loss factor) and $b = 36.5$ mW/rpm (windage loss factor) are fitted from a no load test run on the prototype, upon separation of no-load iron and PM loss.

$$P_{mech} = a\cdot n^3 + b\cdot n \qquad (19)$$

IV. Efficiency Map Computation

A. Description of the procedure

The efficiency map is computed on a torque-speed matrix, with torque organized by rows and speed by columns. Sinusoidal supply is considered, whereas PWM losses will be evaluated in selected operating points to limit the computational burden and validated in the dedicated section VI. The efficiency map evaluation algorithm is organized with two nested loops, see Fig. 8: the outer for the speed levels, with index j, and the inner for the torque levels, with index i.

Besides the flux maps and the loss models introduced in the previous sections, the additional data needed for the evaluation are:

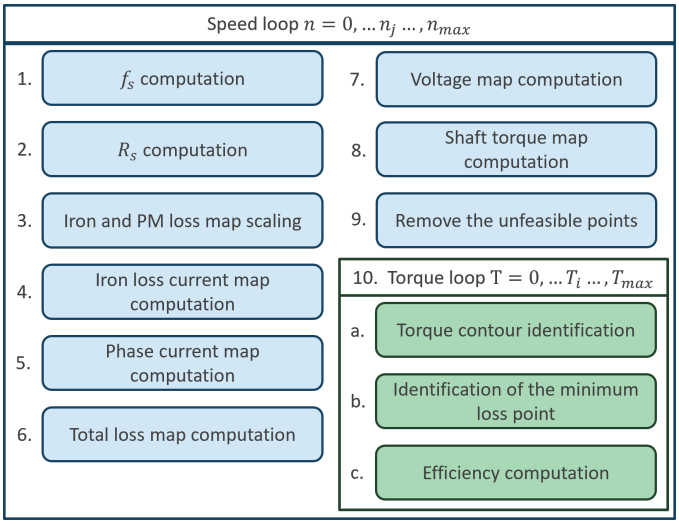

Fig. 8. Efficiency map algorithm flowchart.

- current and voltage limits I_{max} and V_{max};
- phase resistance $R_{s,0}$ at reference temperature $\Theta_{Cu,0}$;
- permanent magnet temperature Θ_{PM};
- winding temperature Θ_{Cu}.

The procedure refers to a maximum efficiency control strategy with voltage and current saturation, which resembles from very close the real-world control strategy based on maximum torque per ampere (MTPA) law at low speed and flux weakening that will be adopted in the experimental validation.

It is convenient to define the element-wise matrix product and division operators "$\odot$"and "$\oslash$". They will be applied to the flux and loss map matrices, function of i_{dq}^m.

The procedure is described step by step.

1) The electrical f_j and angular frequency ω_j are computed at the rotor speed n_j.
2) The stator resistance is computed at f_j (17) and temperature-adjusted (20).

$$R_{s,\Theta} = R_s\cdot[1 + \alpha_{Cu}(\Theta_{Cu} - \Theta_{Cu,0})] \qquad (20)$$

3) The iron and PM loss maps $\mathbf{P}_{Fe}, \mathbf{P}_{PM}$ are computed at f_j as (14) and (15). All the maps in the following refer to f_j.
4) The loss current vector map $\mathbf{I}_{dq}^{Fe}$ is computed as the inverse of (5):

$$\mathbf{I}_{dq}^{Fe} = \left[\frac{2}{3}\cdot(\mathbf{P}_{Fe} + \mathbf{P}_{PM}) \oslash (j\cdot\omega_j\cdot\mathbf{\Lambda}_{dq})\right]^* \qquad (21)$$

5) The total current map $\mathbf{I}_{dq}$ is computed (2). The copper loss map $\mathbf{P}_{Cu}$ is also computed (4).
6) The total loss map $\mathbf{P}_{loss}$ is now evaluated as:

$$\mathbf{P}_{loss} = \mathbf{P}_{Cu} + \mathbf{P}_{Fe} + \mathbf{P}_{PM} + P_{mech} \qquad (22)$$

7) The voltage map $\mathbf{V}_{dq}$ is evaluated from (1).
8) The torque matrix $\mathbf{T}$ is computed from the electromagnetic torque $\mathbf{T_{em}}$ and the mechanical loss, using (7).

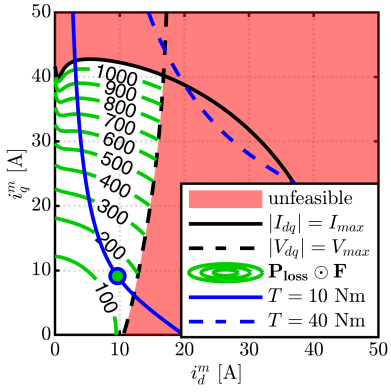

Fig. 9. Graphical explanation of the efficiency map computation on the dq plane at $n_j = 3000$ rpm and $T_i = 40$ Nm (unfeasible point) and $T_i = 10$ Nm (feasible point).

9) All the i_{dq}^m points violating the current and voltage limits are eliminated using the feasibility matrix $\mathbf{F}$ defined as:

$$\begin{cases} \mathbf{F} = NaN & \text{where } |\mathbf{I}_{dq}| > I_{max} \\ \mathbf{F} = NaN & \text{where } |\mathbf{V}_{dq}| > V_{max} \\ \mathbf{F} = 1 & \text{elsewhere} \end{cases} \tag{23}$$

where NaN stands for not a number. All the defined matrices are term-by-term multiplied by $\mathbf{F}$ to eliminated unfeasible points.

10) Here the loop of the torque values starts.
   a) The torque contour $T = T_i$ is extracted from the $\mathbf{T} \odot \mathbf{F}$ map. The result is the family of current coordinates $(i_d^m, i_q^m)_{T_i}$ corresponding to T_i.
   b) From the $(i_d^m, i_q^m)_{T_i}$ family, the minimum loss point is extracted.
   c) Efficiency is finally computed as:

$$\eta_{ij} = \frac{T_{ij} \cdot \frac{\omega_{ij}}{p}}{T_{ij} \cdot \frac{\omega_{ij}}{p} + P_{loss,ij}} \tag{24}$$

The evaluation of the (i_d^m, i_q^m) coordinates of minimum loss for two torque-speed combinations is graphically described in Fig. 9. Two levels of torque (10 and 40 Nm) are considered at $n_j = 3000$ rpm. The point $T_i = 40$ Nm, $n_j = 3000$ rpm is not feasible, abd thus the family $(i_d^m, i_q^m)_{T_i}$ is empty, so the algorithm sets the corresponding efficiency point as NaN. Conversely, if $(i_d^m, i_q^m)_{T_i}$ is not empty like for $T_i = 10$ Nm, the minimum loss i_{dq}^m point (green dot) is determined and used to calculate all the quantities related to the (T_i, n_j) point (voltages, flux linkages, currents, loss terms) from the respective maps.

B. Results

The iron loss map is built upon a 15x15 grid of single-point simulations with 90 rotor positions on 180° electrical degrees of excursion, evaluated in about 60 minutes with the reference workstation. Two temperature conditions are considered:

- cold condition: winding temperature $\Theta_{Cu} = 40$°C and PM temperature $\Theta_{PM} = 20$°C;
- hot condition: winding temperature $\Theta_{Cu} = 130$°C and PM temperature $\Theta_{PM} = 120$°C.

The winding temperature intuitively increases copper loss, with substantial impact in the high torque region. Dealing with the PM temperature, this affects the PM remanence, and, ultimately, the output torque for a given current.
Fig. 10 compares the efficiency maps in cold and hot conditions. As expected, the efficiency is higher in the cold scenario, thanks to the lower phase resistance and the higher PM remanence. The PM temperature slightly affects also the maximum torque (low speed region): the torque produced in hot conditions in slightly lower than the that in cold conditions (difference of 1 Nm).
A low impact of the PM loss on total loss is reported. With reference to the considered efficiency maps, PM loss is lower than 1% of the iron loss for all the operating points. This is specific of the machine under test and not a general finding for interior PM machines.

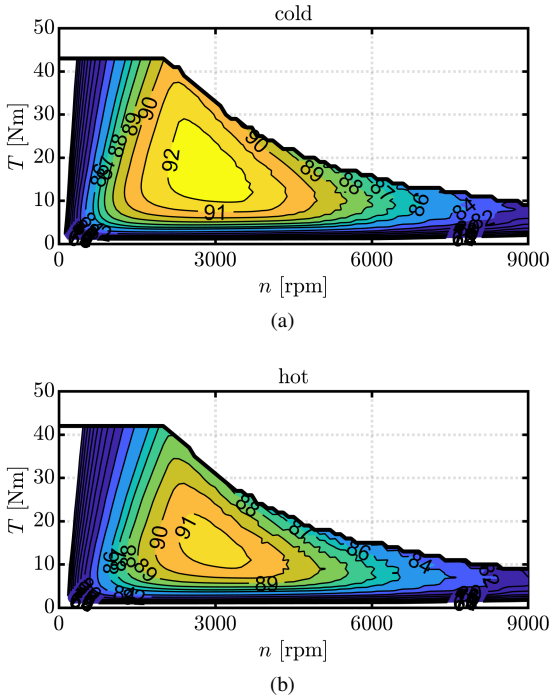

Fig. 10. Efficiency maps of the benchmark motor with maximum efficiency control in cold (a) and hot (b) conditions.

V. Experimental Validation

The experimental validation consists of two steps: flux maps identification at constant speed and efficiency map measurements. The experimental data are first compared to the FEA calculated efficiency map and then to the loss estimation including the PWM effect for selected operating points. Direct flux vector control (DFVC) with MTPA and flux weakening is used for the tests [20].

A. Test Rig and Measurement System Description

The same setup can be adopted for the flux and efficiency maps measurements. It is reported in Figs.11-12 and consists of the prototype (MUT=Motor Under Test) and a Driving Machine (DM). The former is current or torque controlled, while the latter determines the speed of the test. The DM is controlled by its own drive, while the MUT is supplied with a custom-controlled inverter commanded through a dSPACE 1202 MicroLabBox fast prototyping board. The core of the measurement system is the HBM Gen7t data recorder. It collects electrical and mechanical values at 18-bit resolution and 2 MSPS sampling rate. The MUT line voltages are directly measured from the system, while the currents are measured through ULTRASTAB LEM transducers. Dealing with mechanical quantities, shaft torque and speed are measured by a T40B, 200Nm torquemeter by HBM. The MUT position feedback is also acquired from the data logger for the dq transformations.

B. Flux Maps Validation

Flux maps are measured at 300 rpm with the method described in [21] and with a PM temperature equal to 20°C.

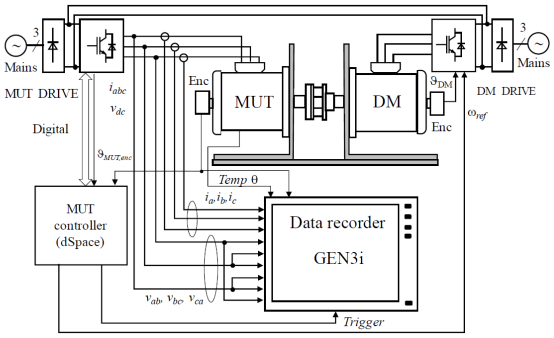

Fig. 11. Schematic of the test-rig setup (from [21])

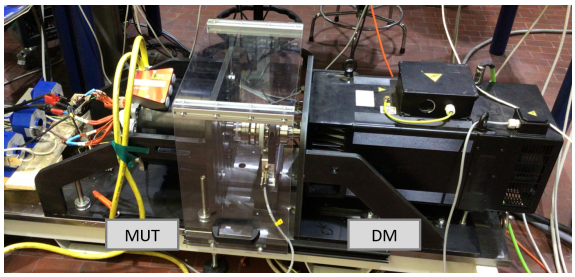

Fig. 12. Picture of the test rig used for the BRUSA motor, introduced in Section VI-A and the benchmark motor. Here, the first was mounted.

The FEA model needs minor adjustments to compensate for mechanical tolerances of the airgap, PM dimensions and ribs dimensions. All such quantities are modified in the FEA model to match the worst case scenario of mechanical tolerances. Fig. 13 compares the results of the FEA model with the experimental findings. The current and flux linkage amplitude versus torque under MTPA conditions are compared showing good agreement. The relative error is below 5% for the current range of interest in operation.

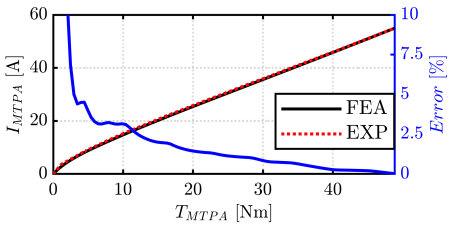

(a)

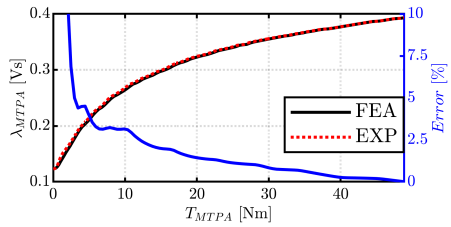

(b)

Fig. 13. MTPA comparison: a) current versus torque and b) flux linkage versus torque for FEA and experimental models.

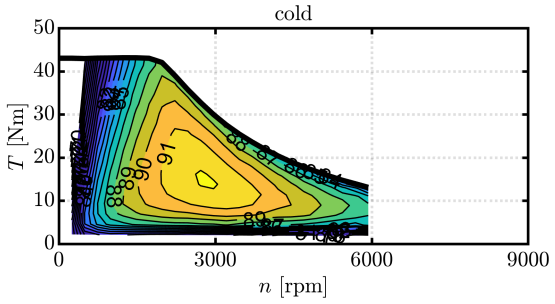

(a)

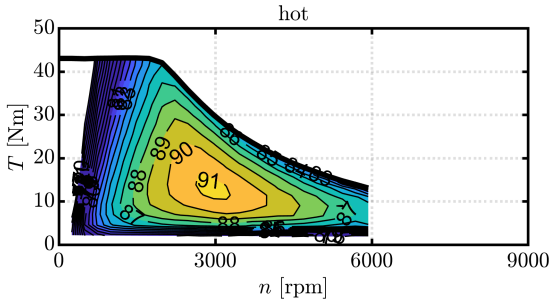

(b)

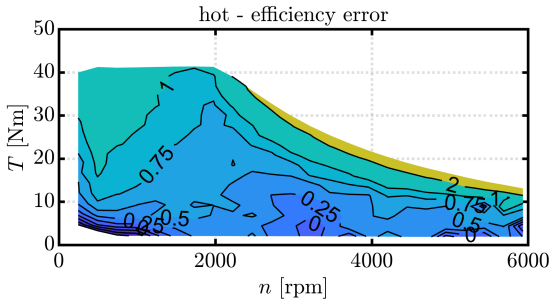

(c)

Fig. 14. Experimental efficiency maps of the benchmark motor in cold (a) and hot (b) conditions evaluated up to 6000 rpm. (c) efficiency error in hot condition respect to the simulated results.

C. Efficiency Maps Validation

Efficiency maps are measured by controlling the MUT torque with DFVC. The experimental flux maps are used in the DFVC flux-observer and for off-line evaluation of the reference MTPA trajectory of the control. Speed is limited to 6000 rpm due to the limitations imposed by the dyno drive. For each reference speed, a reference torque staircase is imposed, and data is recorded for each torque values for a multiple of one mechanical cycle after an appropriate settling time. Before the next torque staircase at the next speed level, a resistance test is performed, by imposing zero speed and controlling the rated torque. The phase resistance measured in DC conditions keeps track of the average winding temperature during the test. A similar test is performed to track the PM temperature, based on the measurement of open-circuit voltage before and after every torque sequence. The maps are measured a first time starting from room temperature conditions (cold map) and then measured again after preliminary heating at 120°C PM temperature (hot map). Due to the relative quickness of

the mapping sequence, the PM temperature rise from the start to the end of the mapping process is negligible altogether (<5°C). The results are shown in Fig. 14. The comparison with Fig. 10 demonstrates a valuable match with the model. The error map in Fig. 14 reports the difference between the measured efficiency and the one obtained with sinusoidal simulations; such a difference can be lessened with an analysis on the PWM effect.

VI. PWM Effect on Loss

In this section, the PWM effect on loss is experimentally investigated and compared to calculations in the one selected operating point, i.e. maximum torque at the maximum tested speed (13 Nm and 6000 rpm). The PWM frequency used in the test is 10 kHz and the DC-link voltage is 280 V. A preliminary no-load test is performed to retrieve the mechanical loss function of speed by way of shaft torque versus speed measurement. For accurate segregation of core and PM loss from mechanical loss, a non-magnetic "dummy" rotor would be required [22], which was not available for this prototype. Being the PM flux linkage of this machine 40% of the rated flux linkage, the iron and PM losses at no-load are considered minor and incorporated into mechanical loss. The core (and PM) loss are segregated as the difference between input and output measured power, minus mechanical and copper loss. It is assumed that copper loss is correctly estimated by the model. PM loss are considered minor in this machine and incorporated into the measured iron loss term. Similarly, the additional PM loss due to PWM is considered negligible due to the relatively low per-unit PWM current ripple, which thus adds a minor loss contribution to the already low PM loss with sinusoidal supply.

The PWM current waveforms are calculated using the circuital model described in the next section, and used to feed a dedicated FEA simulation having a finer time step for iron loss computation. This takes around 10 minutes with the reference workstation for just one operating point, which is considered heavy in the perspective of extending PWM loss computation to the entire efficiency map. The circuital model simulation and copper loss estimation with PWM take less than a minute each.

A. PWM current waveforms

A circuital model of the electric drive is used for the evaluation of the motor currents under PWM supply and field oriented control. The model is implemented in PLECS [9] and it is based on the Voltage Behind Reactance (VBR) approach [23] and the use of flux maps. With reference to Fig.15, the motor is modelled as an RLE load, with a three-phase coupled inductor and controlled voltage generators imposing the back EMF voltage. The coupled inductor term L_s accounts for the dq incremental inductances expressed in abc coordinates, pre-calculated from the dq flux maps, whereas the back-emf voltages are evaluated using the dq flux linkage at the corresponding operating point times the angular frequency in abc coordinates, using again the flux linkage maps. The model is part of the tool syreDrive in the SyR-e platform [24].

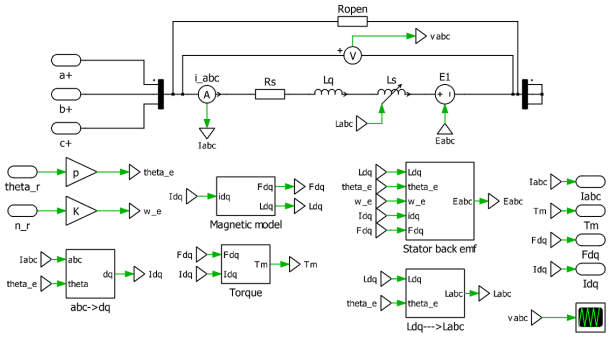

Fig. 15. Circuital model of the PM synchronous machine.

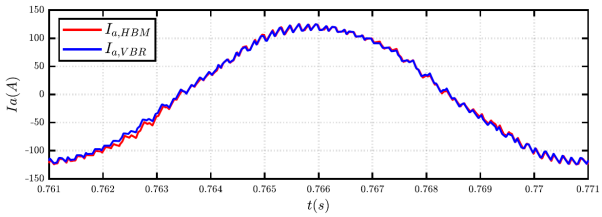

Fig. 16. Measured (red) and simulated (blue) current waveform, Brusa motor.

The accuracy of the circuital model is experimentally validated by comparing the simulated and measured waveforms in steady-state conditions. The tests were performed using the commercial automotive motor Brusa HSM1-6.17.12 [25], rated 130 Nm and 70 kW peak, and with a maximum speed of 12000 rpm.

The measured and simulated current of phase a is shown for the Brusa motor in Fig. 16 in steady state conditions at 2000 rpm to assess the accuracy of current waveform evaluation from the circuital model.

The same approach is used for the motor under test (Table I and Fig. 1) in the specified test conditions, to feed the loss model as said.

B. PWM iron loss validation

To account for the PWM effect, the simulation time step is selected according to the switching frequency. For the case study, the switching time is 100 μs, and a time step of 7 μs is sufficient. Such a time step corresponds to 0.5° electrical degrees, thus the simulation is executed with 360 rotor positions on 180° electrical degrees of excursion.

As reported in Fig. 17, the iGSE method without DC bias effect estimates 447 W of loss with sinusoidal excitation and 454 W under PWM supply. As expected, the increase given by the extra minor loops (hysteresis) and flux density harmonics (eddy current) is limited. However, considering the DC bias effect (iGSE + k_{DC} method), the estimated loss under sinusoidal and PWM supply respectively are equal to 480 and 504 W. In the experimental test, the estimated iron loss is 562 W; the difference with respect to the iGSE + k_{DC} and PWM estimate of 504 W is the metric of loss estimate error. More in general, the comparison of the FEA and experimental efficiency maps shows a 20% increase between SIN and experimental iron loss, hence suggesting correction

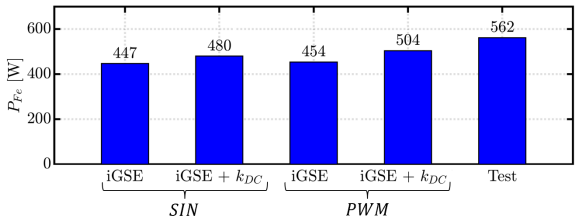

Fig. 17. Iron loss result comparison at 13 Nm and 6000rpm

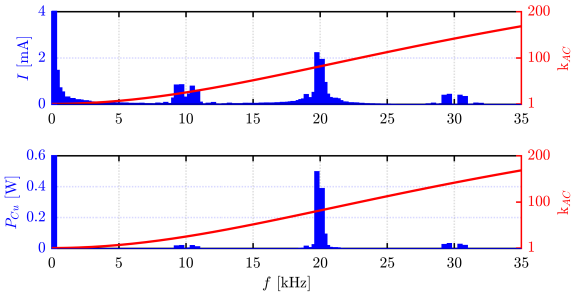

Fig. 18. Current and copper loss harmonic contents at 13 Nm and 6000rpm.

factor could of 1.2 to be applied to the FEA computed iron loss map to match the measurements. Actually, this is in line with the common practices of electric motors manufacturers, which use correction factors between 1.4 and 1.8. For the sake of clarity, no correction coefficient was applied to the results presented in the paper.

C. PWM copper loss

With reference to section III-E, the k_{AC} factor is computed up to 35 kHz and at $\Theta_{Cu} = 40°$C. Fig. 18 shows the FFT spectrum of the current waveform and the corresponding copper loss for each harmonic order. The AC factor is reported in red in the same figure, in p.u. respect to the DC value. Note that even if the k_{AC} reaches high values, greater than 200, the corresponding P_{Cu} is not relevant due to low current amplitudes. Moreover, the highest harmonics loss is at double the switching frequency, i.e. 20 kHz. Finally, Fig. 19 displays the comparison of copper loss under DC, sinusoidal (SIN) and PWM supplies. Not surprisingly, the skin effect on this type of windings has not a significant impact on loss: the increase between extreme conditions DC and PMW is 15 W.

VII. Conclusion

The paper formalizes the approach for the efficiency map computation of synchronous machines. The process is based on FEA calculated flux and loss maps, obtained with the freeware 2D magneto-static software FEMM. A number of assumptions is made for taking into account three-dimensional effects, AC and PWM winding losses, minor loops and PMW loss in the iron, keeping in mind the trade off between accuracy and computational time. Computed and measured efficiency maps are compared, demonstrating the good accuracy of the procedure and suggesting a correction factor of +20% of calculated iron loss, which is considered acceptable and

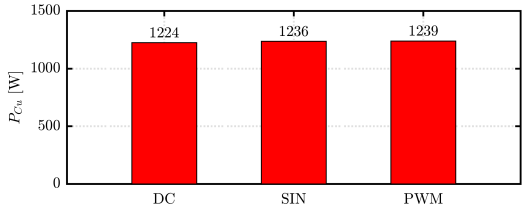

Fig. 19. Copper losses result comparison at 13 Nm and 6000rpm.

competitive with respect to the safety factors commonly in use within the industry. PM loss is evaluated conservatively and practically overlooked in this study, for being very minor for the considered PM-SyR motor test case. More insight would be needed for machines with solid magnets simulated with magneto-static FEA, which is ground for future work. A dedicated section deals with the effects of PWM supply, from the calculation of the phase current waveform, to the iron and copper loss determination. Although the reference motor demonstrated a low increase of loss due to the relatively small PWM current ripple, the computed iron loss are corroborated by the experimental findings. The presented procedure is included in the open-source design suite SyR-e in the form of accessible Matlab functions.

Acknowledgments

The research has been conducted with the support of Power Electronics Innovation Center (PEIC) of Politecnico di Torino. The authors gratefully acknowledge the contribution of Andrei Bojoi, M.Sc. student of Politecnico di Torino, to the dynamic circuital model.

References

[1] A. Krings and C. Monissen, "Review and Trends in Electric Traction Motors for Battery Electric and Hybrid Vehicles," in *2020 International Conference on Electrical Machines (ICEM)*, vol. 1, Aug. 2020, pp. 1807–1813, iSSN: 2381-4802.

[2] N. Bianchi, S. Bolognani, E. Carraro, M. Castiello, and E. Fornasiero, "Electric Vehicle Traction Based on Synchronous Reluctance Motors," *IEEE Transactions on Industry Applications*, vol. 52, no. 6, pp. 4762–4769, Nov. 2016.

[3] C. He and T. Wu, "Analysis and design of surface permanent magnet synchronous motor and generator," *CES Transactions on Electrical Machines and Systems*, vol. 3, no. 1, pp. 94–100, Mar. 2019.

[4] Y. Yang, S. M. Castano, R. Yang, M. Kasprzak, B. Bilgin, A. Sathyan, H. Dadkhah, and A. Emadi, "Design and Comparison of Interior Permanent Magnet Motor Topologies for Traction Applications," *IEEE Transactions on Transportation Electrification*, vol. 3, no. 1, Mar. 2017.

[5] J.-R. Riba, C. López-Torres, L. Romeral, and A. Garcia, "Rare-earth-free propulsion motors for electric vehicles: A technology review," *Renewable and Sustainable Energy Reviews*, vol. 57, May 2016.

[6] I. Boldea, L. N. Tutelea, L. Parsa, and D. Dorrell, "Automotive Electric Propulsion Systems With Reduced or No Permanent Magnets: An Overview," *IEEE Transactions on Industrial Electronics*, vol. 61, no. 10, pp. 5696–5711, Oct. 2014.

[7] J. O. Estima and A. J. Marques Cardoso, "Efficiency Analysis of Drive Train Topologies Applied to Electric/Hybrid Vehicles," *IEEE Transactions on Vehicular Technology*, vol. 61, no. 3, Mar. 2012.

[8] S. Ferrari, P. Ragazzo, G. Dilevrano, and G. Pellegrino, "Flux-Map Based FEA Evaluation of Synchronous Machine Efficiency Maps," in *2021 IEEE Workshop on Electrical Machines Design, Control and Diagnosis (WEMDCD)*, Apr. 2021, pp. 76–81.

[9] Plexim, "PLECS." [Online]. Available: https://www.plexim.com/products/plecs

[10] F. Cupertino and G. Pellegrino, "SyR-e: Synchronous Reluctance (machines) - evolution." [Online]. Available: www.github.com/SyR-e

[11] D. Meeker, "FEMM: Finite Element Method Magnetics." [Online]. Available: www.femm.info

[12] G. Y. Sizov, D. M. Ionel, and N. A. O. Demerdash, "Modeling and Parametric Design of Permanent-Magnet AC Machines Using Computationally Efficient Finite-Element Analysis," *IEEE Transactions on Industrial Electronics*, vol. 59, no. 6, pp. 2403–2413, Jun. 2012.

[13] I. Sirotić, M. Kovačić, and S. Stipetić, "Methodology and Measurement Setup for Determining PWM Contribution to Iron Loss in Laminated Ferromagnetic Materials," *IEEE Transactions on Industry Applications*, vol. 57, no. 5, pp. 4796–4804, Sep. 2021.

[14] M. Lancarotte, C. Goldemberg, and A. d. A. Penteado, "Estimation of FeSi Core Losses Under PWM or DC Bias Ripple Voltage Excitations," *IEEE Transactions on Energy Conversion*, vol. 20, no. 2, Jun. 2005.

[15] K. Venkatachalam, C. Sullivan, T. Abdallah, and H. Tacca, "Accurate prediction of ferrite core loss with nonsinusoidal waveforms using only Steinmetz parameters," in *2002 IEEE Workshop on Computers in Power Electronics, 2002. Proceedings.* Mayaguez, Puerto Rico: IEEE, 2002.

[16] D. Jiles and D. Atherton, *Theory of ferromagnetic hysteresis*, ser. J. Magn. Magn. Mater., 1986, vol. 61, no. 1-2.

[17] K. Yamazaki, Y. Sato, and K. Terauchi, "Loss Analysis of Induction Motors Fed by Inverters by Using Simple Models of Major and Minor Hysteresis Loops in Stator and Rotor Cores," in *2021 IEEE Energy Conversion Congress and Exposition (ECCE)*, Oct. 2021, pp. 4135–4141, iSSN: 2329-3748.

[18] C. Simao, N. Sadowski, N. J. Batistela, and J. P. A. Bastos, "Evaluation of Hysteresis Losses in Iron Sheets Under DC-biased Inductions," *IEEE Transactions on Magnetics*, vol. 45, no. 3, pp. 1158–1161, Mar. 2009.

[19] L. Chang, W. Lee, T. M. Jahns, and K. Rahman, "Investigation and Prediction of High-Frequency Iron Loss in Lamination Steels Driven by Voltage-Source Inverters Using Wide-Bandgap Switches," *IEEE Transactions on Industry Applications*, vol. 57, no. 4, pp. 3607–3618, Jul. 2021.

[20] G. Pellegrino, R. I. Bojoi, and P. Guglielmi, "Unified Direct-Flux Vector Control for AC Motor Drives," *IEEE Transactions on Industry Applications*, vol. 47, no. 5, pp. 2093–2102, Sep. 2011.

[21] E. Armando, P. Guglielmi, G. Pellegrino, and R. Bojoi, "Flux linkage maps identification of synchronous AC motors under controlled thermal conditions," in *2017 IEEE International Electric Machines and Drives Conference (IEMDC)*. Miami, FL, USA: IEEE, May 2017, pp. 1–8.

[22] S.-H. Park, E.-C. Lee, G.-J. Lee, S.-O. Kwon, and M.-S. Lim, "Effect of Pole and Slot Combination on the AC Joule Loss of Outer-Rotor Permanent Magnet Synchronous Motors Using a High Fill Factor Machined Coil," *Energies*, vol. 14, no. 11, p. 3073, May 2021.

[23] S. Pekarek, O. Wasynczuk, and H. Hegner, "An efficient and accurate model for the simulation and analysis of synchronous machine/converter systems," *IEEE Transactions on Energy Conversion*, vol. 13, no. 1, pp. 42–48, Mar. 1998.

[24] A. Varatharajan, D. Brunelli, S. Ferrari, P. Pescetto, and G. Pellegrino, "syreDrive: Automated Sensorless Control Code Generation for Synchronous Reluctance Motor Drives," in *2021 IEEE Workshop on Electrical Machines Design, Control and Diagnosis (WEMDCD)*, Apr. 2021, pp. 192–197.

[25] "HSM1-6.17.12 – BRUSA." [Online]. Available: https://www.brusa.biz/portfolio/hsm1-6-17-12/?lang=en